Jetting and droplet formation of particle-loaded fluids

Jing Shi ; Neil Cagney ; John Tatum; Angus Condie ; J. Rafael Castrejón-Pita

Check for updates

View Online

Export Citation

AIP Publishing

Jetting and droplet formation of particle-loaded fluids

View Online   Export Citation   CrossMark

Jing Shi,[1,2] (iD) Neil Cagney,[1] (iD) John Tatum,[2] Angus Condie,[2] (iD) and J. Rafael Castrejón-Pita[3,a] (iD)

AFFILIATIONS

[1]School of Engineering and Materials Science, Queen Mary University of London, London E1 4NS, United Kingdom
[2]Xaar, 3950 Cambridge Research Park, Waterbeach, Cambridge CB25 9PE, United Kingdom
[3]Department of Mechanical Engineering, University College London, London WC1E 7JE, United Kingdom

[a]Author to whom correspondence should be addressed: r.pita@ucl.ac.uk

ABSTRACT

Inkjet printing is an attractive method for patterning and fabricating objects across many areas of industry. There is a growing interest in the printing of inks with high particle-loading, such as inks containing glass frit, ceramic and functional inks. However, the use of these inks is often limited due to uncertainty regarding the impact of their rheology on the printing process. Understanding of the role of complex rheology in the jetting of loaded inks is therefore needed to facilitate the wider application of inkjet printing. Here, we characterize the complex rheology and the jetting of model dispersion inks (containing 10, 15, and 23 vol. % TiO_2 nanoparticles) and compared them with those without particles. The jetting of the model fluids was conducted with a commercial inkjet printhead (nozzle diameter 34 μm) and visualized with stroboscopic and ultra-high-speed imaging. For low particle concentrations, droplet formation is generally similar to those of unloaded inks, provided their Ohnesorge number and Weber number are matched, although the filament of the loaded model fluid tends to have earlier break-off, having a shorter length. The jetting reliability decreased with increase in particle-loading until reliable jetting can no longer be achieved, due to local particle–particle interactions in the ink channel and in the filament during the fast extensional thinning process. A jetting map is presented which illustrates the influence of particle-loading on the droplet formation, and indicates that the acceptable range of Ohnesorge number for jetting is reduced as the particle-loading is increased.

I. INTRODUCTION

Drop-on-demand (DOD) inkjet printing deposits precise quantities of inks, in the form of picolitre droplets, on an arbitrary surface when required. It is a versatile method for patterning and fabricating objects due to the advantages brought by the controlled, additive, and non-contact production process. Two primary types of DOD inkjet technologies exist—thermal and piezoelectric inkjet. In thermal inkjet printing, a thin layer of ink (in immediate contact of a small thin-film heater) is heated within the nozzle chamber, forming a vapor bubble that, in turn, produces a pressure pulse in the fluid causing ink in the nozzle to be ejected. In piezoelectric inkjet printing, a voltage waveform excites a piezoelectric transducer deforming the wall(s) of the ink channel creating a pressure pulse, causing the ejection of ink from the nozzle. In recent years, inkjet printing has demonstrated applicability in different areas such as ceramics,[1–3] electronics,[4–10] 3D printing and rapid prototyping,[11,12] biosensors,[13] hydrophobic substrates fabrication,[14] fabrication of uniform polymeric particles,[15] and tissue engineering.[16–18] The wide application of inkjet printing is, however,

largely limited by the ink's rheological properties. Understanding of the role of complex rheology in the jetting of functional and/or complex inks is needed to facilitate the wider application of inkjet printing.

In 1984, Fromm[19] used dimensionless numbers to parametrize the fluid physical properties and solved the Navier–Stokes equations for the flow dynamics of droplet ejection. Fromm identified that the ratio of the Reynolds number (Re) to the square root of the Weber number (We), a quantity called the Z number by some later studies, can be used to predict the formation of stable droplets. The Z number is mainly adopted in the field of inkjet printing; it is the inverse of the Ohnesorge number (Oh), which is more widely used in fluid mechanics ($Oh = 1/Z$). Another relevant dimensionless number is the capillary number (Ca). The aforementioned dimensionless numbers are defined as

$$Re = \frac{\rho V a}{\mu}, \tag{1}$$

$$We = \frac{\rho V^2 a}{\sigma}, \tag{2}$$

$$Oh = \frac{1}{Z} = \frac{\mu}{\sqrt{\rho \sigma a}}, \tag{3}$$

$$Ca = \frac{\mu V}{\sigma}, \tag{4}$$

where ρ, μ, σ, V, and a are the droplet's density, dynamic viscosity, surface tension, velocity, and characteristic dimension (often the radius or diameter), respectively. Indeed, Fromm[19] predicted that stable drop formation in DOD systems occurs when $Oh < 0.5$ ($Z > 2$). Derby and Reis in 2003[20] reported that commercial DOD printable fluids typically exists in the range of $0.1 < Oh < 1$ ($1 < Z < 10$). Jang et al. in 2008,[21] using a noncommercial inkjet system (Microfab printhead), defined the printable range as $0.07 < Oh < 0.25$ ($4 < Z < 14$), by considering properties, such as single droplet formability, positional accuracy, and maximum allowable jetting frequency. In brief, the upper limit of Oh is dominated by the viscous dissipation of the pressure pulse produced by the actuator, the higher the viscosity the harder to eject and form a drop. At high Oh, the jetting is typically achieved by higher driving voltages on the piezoelectric driver and often results in droplets with long filaments. At the lower limit of Oh, an unacceptable number of satellite droplets are formed as well as unreliable jetting caused by the reduced damping of the meniscus. It is noted that the experimentally obtained limits of Oh are dependent on the inkjet systems, as they are affected by the energy requirements (acoustics, piezoelectric geometry and other characteristics), and the jetting frequency.[22] Furthermore, the characteristic dimension for free surface jet flows is not consistent in the literature; the early studies of Fromm,[19] Derby and Reis,[20] and Jang et al.[21] used the nozzle radius as the characteristic length, while some later studies[23–25] used the orifice diameter. Consequently, a factor of 2 for We or $1/\sqrt{2}$ for Oh is encountered between data using diameter instead of the radius. Nevertheless, the limits of Oh for jettable fluids have been widely used as an approximate guide. In this study, we used the orifice diameter as the characteristic length. Derby in 2010 assumed a number of conditions for printability: the droplet must possess sufficient kinetic energy to be ejected from the nozzle ($We > 4$); conditions must be below the onset of splashing ($We^{1/2}Re^{1/4} < 50$); and the fluid Ohnesorge number must be within an acceptable range (i.e., $0.1 < Oh < 1$).[26] These conditions result in a map with coordinates of Re and We that shows the domain of reliable DOD printing. This map has since been widely accepted as a guide for developing inks suitable for DOD printing. Equivalent regions have been proposed by McKinley and Renardy,[27] and Lohse[28] where the map is seen in terms of Re and Oh. Liu and Derby in 2019 experimentally investigated the boundaries for stable inkjet-droplet formation and proposed a map with coordinates of the Weber number of the fluid jet, We_j (calculated with the fluid jet velocity in the drop generator prior to drop formation and detachment, instead of the drop velocity) and Oh; stable drop generation was found at $2 < We_j < 25$ and $0.05 < Oh < 0.5$.[29] It worth noting that all the aforementioned maps assume that the fluid behaves in a Newtonian manner, requiring adjustments for complex fluids such as polymer solutions or dispersed particles.

Studies on the inkjet printing of complex fluids have been mostly focused on dilute solutions of polymers. Shore and Harrison[30] in 2005 showed that the addition of a minute quantity of high molecular weight polymer to a low viscosity Newtonian solvent leads to the jetting of a longer thread, a longer breakup time, a lower velocity, and fewer satellite drops than Newtonian fluids of similar shear viscosity.

The role of polymer molecule topology in filament formation during inkjet printing of dilute polymer solutions was examined by de Gans et al., who observed longer filaments for inks containing linear polymers compared to those containing star polymers,[31] which they attributed to the polymers' coil-stretch transition during filament formation. Hoath et al. in 2009 investigated the link between the rheological properties and the jetting characteristics of viscoelastic fluids containing linear polymers with various molecular weights.[32] They found no correlation between the low shear viscosity and the jetting behaviors, but observed a linear correlation between the high-frequency rheological properties and the jet breakup time. Hoath et al. in 2012 presented a model for stretching ligaments of polymer solutions during the ejection process of inkjet printing.[33] The model predicts three different regimes of jetting behaviors depending on the jet Weissenberg number Wi ($Wi = \tau V/l$, where τ is the relaxation timescale, and l the ligament length). The three regimes are the Newtonian regime ($Wi < 1/2$), the viscoelastic regime ($1/2 < Wi < L$, where L represents the polymer extensibility, defined as the ratio of the maximum length of the polymer chain to its equilibrium diameter), and the fully extended polymer regime ($Wi > L$). Yoo and Kim in 2013 experimentally investigated the generation of inkjet droplets of shear-thinning viscoelastic Xanthan gum solutions and showed that the ejection process is primarily controlled by the high or infinite shear viscosity, while the detachment process is controlled by the extensional viscosity.[34]

Compared to the case of polymer solutions, drop formation of particle-loaded inks has not received much attention to date. Some studies have focused on specific applications such as ceramic[1,2,35,36] and electronics fabrication.[5,6,37] The basic ink formulations reported for industrial applications in general consist of a solvent or mixture of solvents, a dispersant or combination of dispersants (polymeric type for most cases) and nano-particles [mean particle size of $O(10)$ nm for electronics fabrication and $O(100)$ nm for ceramic fabrication]; some also include one or more functional additives (short-chain organic compounds). Nallan et al. developed a jettability window within the Ca–We space together with limits of Z for nanoparticle-based inkjet inks. This jettability window does not account for the influence of particles as it is based on their tests with dilute dispersions ($\sim$5 vol. % nanoparticles of mean diameter 2–3 nm) which behave largely as Newtonian fluids.[25] Wang et al.[38] studied the DOD drop formation dynamics for model inks including a Newtonian liquid and shear-thinning colloidal dispersions (with 5.7 and 15 vol. % pigment loadings). Their results showed that there is a great deal of similarity under ideal jetting conditions, but obtaining good jetting in the colloidal dispersion case is much more difficult than in a simple liquid. Non-straight flying trajectory, non-axisymmetric ligament formation or inconsistent jetting were observed for the colloidal inks and the authors attributed the poor jetting to the accumulated particles and non-ideal wetting condition on the nozzle plate.

Traditional disperse dye or pigment inks used for the printing of graphics typically contain 5–10 vol. % solids. Higher particle-loading inks have advantages such as higher thickness-to-width (or aspect) ratio, higher efficiency to build up materials, better functionality, and less energy for drying (if needed). However, it is more challenging to develop stable high particle-loading dispersions that are suitable for inkjet printing as particles tend to self-associate via short-range van der Waals attractive forces, bringing in complex rheological properties.[39] Our study aimed to explore the influences of high particle-loading

on the rheological properties of the dispersions and the DOD droplet formation of particle-loading fluids for industrial applications.

Visualizing the jetting process from an inkjet system to obtain detailed information of the filament stretching and breakup is challenging due to the fast jetting velocity and the size of droplets and filaments.[40] Stroboscopic techniques with very short illumination times to freeze the motion of the droplets are the most common method. The jetting process can be monitored by varying the time delay between the signals to the printhead and the strobe. This procedure relies on the repeatability of drop formation to give the impression that one is observing individual jets and drops. Inkjet printing is largely very uniform and reliable, making this an effective visualization technique. However, for non-Newtonian fluids, the reproducibility is not as good as in the case of Newtonian fluids. Alternatively, ultra-high-speed imaging can be used, but the pixel resolution at the required frame rates is typically poor. In our study, both the stroboscopic technique and ultra-high-speed imaging were applied. The stroboscopic technique facilitated the development of the optimal waveform for an individual ink. It was also used to study the droplet formation process for reliable jetting cases with an image resolution as high as 0.26 μm/pixel. With a ultra-high-speed camera, the formation of individual droplets were captured at a high temporal resolution of 580 000 fps and an image resolution of 0.67 μm/pixel. This is particularly useful for the highly loaded fluids when the jetting becomes less reliable. To fully evaluate the rheological properties of our model fluids, we used different rheology measurement techniques, including measuring the shear rheology with a traditional rheometer, complex rheology with a piezoaxial vibrating (PAV) rheometer and extensional rheology with a filament stretching device. A systematic study was conducted by developing model dispersions containing different particle-loadings (10, 15, and 23 vol. %) characterizing the rheological properties of the model dispersion inks and their jetting behaviors, and comparing the jetting behaviors of the unloaded model fluids with those of the unloaded fluids. The jetting of droplets at a range of Ohnesorge and Weber numbers ($Oh = 0.13$–1.44, $We = 16$–44) were investigated. The influences of particle-loading on extensional rheology, jetting reliability, and droplet formation dynamics were demonstrated and discussed.

II. MATERIALS AND EXPERIMENTS
A. Materials and sample preparation

The unloaded model fluids used in this study are mixtures of glycerol (Sigma-Aldrich), ultrapure water (Millipore), 5 wt. % 2-butoxyethanol, and 0.2 wt. % water disinfectant (Aqua-stabil, Julabo). Various glycerol concentrations were tested, including 60, 70, and 75 wt. %. The loaded model fluids used are dispersions of TiO_2 nanopowder in aqueous solution. The TiO_2 nanopowder (Ti-Pure[TM] R-902+, Chemours) has the following particle size distribution percentile values: D50 $\sim$ 400 and D90 $\sim$ 600 nm, where D50 and D90 indicate the size below which 50% and 90% of all particles are found, respectively. The dispersions were stabilized using a commercial polymeric dispersant (DISPERBYK-2015, BYK); the amount of the dispersant added was 7.5 wt. % of the particle-loadings. 5 wt. % Polyethylene glycol (PEG) 4000 was used as a co-solvent in addition to ultrapure water to increase the fluid viscosity and 10 wt. % diethylene glycol (DEG) was added as humectant to prevent nozzle drying and clogging. In addition, 0.2 wt. % water disinfectant was added to prevent bacteria formation. Dispersions of three different particle-loadings—10, 15,

and 23 vol. % (or 30, 40, and 54 wt. %)—were tested. These values of volume fraction lie in the semi-dilute regime, in which the suspension rheology is expected to remain approximately Newtonian.[41]

To prepare the dispersions, PEG 4000 was first gradually added into DEG at an elevated temperature of 150 °C under magnetic stirring to form a homogeneous mixture of PEG 4000/DEG (weight ratio at 1:2). The dispersant and the water disinfectant were dissolved in ultrapure water. The mixture of PEG4000/DEG was further mixed with water containing dispersant and disinfectant. The appropriate amount of TiO_2 powder was further gradually added into the above aqueous solution under stirring using a disperser (Dispermat SR, VMA-GETZMANN); the dispersion was further dispersed at a high speed of 10 000 rpm for 30 min. Once prepared, the dispersions were stored under slow magnetic stirring to prevent sedimentation of particles. The rheological properties of the dispersions were found to be consistent within a month. The characterization of the model fluids and following jetting tests were completed within 2 weeks to make sure that the fluid properties were consistent throughout the tests.

B. Characterization of model fluids

The size of the particles in the prepared dispersions was checked with Mastersizer 3000 (Malvern Panalytical), which indicated there was a very small portion of aggregates with a higher D90 $\sim$1.0 μm but similar D50 $\sim$400 nm. Observation of the dispersions under a microscope also showed that the particles were in general well dispersed having few larger particles.

The shear rheology of the model fluids was measured at various temperatures using a Discovery HR10 rheometer (TA Instruments) with a cone (40 mm diameter, 1° angle) and plate geometry. The shear viscosity profile of a fluid under steady shear (shear rate 10–2000 s^{-1}) was obtained. A piezoaxial vibrating (PAV) rheometer (TriPAV, TriJet) was used to measure the complex rheology of the model fluids with frequency up to 10 000 Hz. A filament stretching device (Trimaster, TriJet) was used to explore the extensional rheology of the model fluids. The surface tension was measured by a EZ-PI Plus tensiometer (Kibron) and the density was measured with a DSA 5000M (Anton Paar). A range of temperatures, 25–40 °C, were considered in order to adjust the Ohnesorge number of the fluids. The glycerol mixtures with different glycerol concentrations and at different temperatures have viscosities 5–66 cP, densities 1.14–1.20 g/cm^3, and surface tensions 32.0–35.8 mN/m. The dispersions with different particle-loadings and at different temperatures have viscosities 6–40 cP, densities 1.30–1.76 g/cm^3, and surface tensions 42.0–45.3 mN/m. More discussions of the rheological properties of the model fluids are presented in Sec. III A.

C. Jetting experiments

The model fluids were jetted using a drop-on-demand printhead (Xaar 1003 GS12, Xaar). The printhead has two rows of nozzles, each row having 500 nozzles spaced at a pitch of 141 μm. The nozzles have a diameter of 34 μm. The printhead features a piezoelectric actuator with shared wall architecture and consequently three-cycle jetting.[42] Multiple actuations in rapid succession in the same channel can take place before firing, enabling drops of varying subdrops (or dpd, dropper-dot) by controlling the number of actuations. An ink supply system (Hydra Ink Supply System, Xaar) with an external ink reservoir

04 June 2024 13:58:28

with inks under consistent magnetic stirring was used together with the printhead. The ink is recirculated through the complete fluid path using pumps in the supply and return fluid paths [Fig. 1(a)]. The temperature of the ink can be controlled to be between the ambient temperature and 50 °C with heaters on the supply pipe. The pumps and heaters are controlled by feedback from sensors located in a sensor manifold connected above the printhead. In this study, the jetting and formation of 3-dpd drops at a jetting frequency of 3000 Hz were experimentally investigated; most jetting tests were conducted with ink temperature of 25 °C and some tests at varying temperatures up to 45 °C. Optimized pull-push waveforms for the model fluids were used. The driver was adjusted to achieve several different drop velocities, namely ∼4.0, 5.0, and 6.0 m/s, at ∼1.0 mm printing distance. Detailed operating parameters of the jetting tests are listed in Table I.

The schematic views of the experimental setups for visualizing the jetting and droplet formation are shown in Fig. 1. A stroboscopic imaging system [Fig. 1(a)] and a high-speed imaging system [Fig. 1(b)] were setup in parallel and the printhead, which was located on a three-dimensional stage, can move between the two imaging systems. The stroboscopic imaging system consisted of a LED, a lens for light focusing onto the plane of the jetting drops, a CCD camera (Manta G-282, 2.8 MP) and zoom lenses (variable magnification) and adaptors for the camera. A lower magnification, which allows for a field of view of about 1.7×1.3 mm and imaging the jetting of 12 nozzles at a resolution of 0.88 μm/pixel, was used for developing the waveform for a model fluid; double strobes with a delay of 10 or 15 μs were used to check the drop velocity at ∼1 mm printing distance by measuring the distance traveled between known LED trigger delays. Once an optimized waveform was developed, the jetting process was further imaged using a higher magnification (0.26 μm/pixel with an effective $14 \times$ magnification) and a sequence of delayed strobe light (pulse width at 0.21 μs) with an interval of 1 μs; this procedure relies on the repeatability of drop formation. The high-speed imaging system consisted of a metal halide light source (PhotoFluor II, 89 North), a light
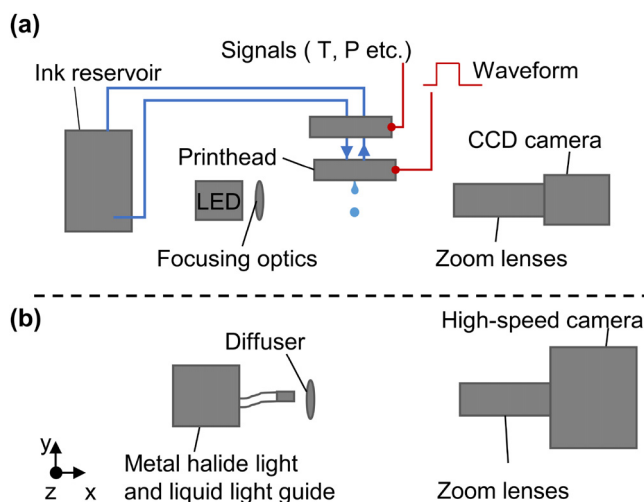

FIG. 1. A schematic of the experimental setup. A stroboscopic imaging system (a) and a high-speed imaging system (b) are setup in parallel along the z axis (perpendicular to the plane of the paper). The printhead is located on a three-dimensional stage, thus can move between the two imaging systems.

diffuser, a high-speed camera (TMX 5010, Phantom) and zoom lenses and adaptors for the camera. The jetting of individual droplets was recorded with the high-speed camera at 580 000 fps and shutter 0.1 μs, and the image resolution achieved was 0.67 μm/pixel.

III. RESULTS

A. Rheology of model fluids

The shear viscosities of the loaded model fluids with different particle-loadings, and unloaded model fluids with different glycerol concentrations are shown in Figs. 2(a) and 2(b), respectively. As expected, the shear viscosity of the loaded model fluids increases as particle-loading increases. The shear viscosity was virtually constant against the shear rate for both the unloaded and loaded model fluids, indicating Newtonian behaviors. For an individual model fluid, the shear viscosity decreases when the temperature increases. Some comparable viscosities were obtained for the unloaded and loaded fluids by controlling the temperatures. In our following jetting tests, the jetting temperature were controlled to examine the jetting behaviors at comparable viscosities or dimensionless numbers (Oh and We).

The viscoelastic moduli of the model fluids at 25 °C, measured by the PAV rheometer, are shown in Fig. 3. The elastic modulus, G', was negligible for both the unloaded and loaded model fluids. This indicates that both the loaded and unloaded model fluids have little linear elasticity.

Figures 4(a)–4(c) shows the filament stretching, thinning and breakup for fluids with various particle-loadings. The initial sample placed between a pair of pistons has an initial diameter $D_0 = 1.0$ mm and a height $h_0 = 0.5$ mm. The sample was rapidly stretched to 1.2 mm by moving each piston 0.35 mm apart at a relative stretching velocity of 200 mm/s. The deformation of a sample during stretching is approximately axisymmetric about the midplane as expected, because the influence of gravity is negligible with the Bond number ($Bo = \rho g R_o^2/\sigma$, the ratio of gravitational forces to surface tension forces) being $O(10^{-2})$. Here, $t = 0$ ms denotes the time when the pistons stop and after that self-thinning of the liquid bridge occurs, leading to final breakup. For the model fluids with lower particle-loadings, the filament pinched off at both ends of the filament, leading to the formation of a central drop [see Figs. 4(a) and 4(b)]; this kind of thinning is typical for a Newtonian fluid.[43–45] Similar characteristics of filament thinning and breakup were observed for the low to moderate viscous unloaded model fluids. A marked difference in the way the filament thinned and broke was observed for the model dispersion with the highest particle-loading of 23 vol. %. As shown in Fig. 4(c), the filament broke at mid-filament position instead of end-pinching and after that the broken tails moved toward the fluid reservoir on each piston under capillary forces and no droplets were formed. This behavior has been reported for polymer solutions and often indicates the existence of elasticity and/or a high extensional viscosity.[43–45] We note that the complex rheology results of this model fluid from the dynamic squeeze flow rheometer do not indicate any linear elasticity. It is likely that there is some (nonlinear) elastic response caused by the local particle–particle interactions under high extensional strain when the filament became very thin. It has been reported that the way a filament stretches can be used to identify nonlinear viscoelasticity effects that the PAV is not able to detect.[32,46]

By tracking the mid-filament diameter after the cessation of stretching in Fig. 4, the profile of the normalized mid-filament

TABLE I. Operating parameters of jetting tests.

Particle loading[a] (vol. %)	Glycerol concentration[b] (wt. %)	T (°C)	V[c] (m/s)	μ (cP)	ρ (g/cm^3)	σ (mN/m)	Oh	We	Re
…	60	25	4.4	12.9	1.15	32.1	0.36	24	13
…	60	25	5.0	12.9	1.15	32.1	0.36	30	15
…	60	25	6.0	12.9	1.15	32.1	0.36	45	18
…	60	35	4.1	8.5	1.14	32.1	0.24	20	19
…	60	35	5.9	8.5	1.14	32.1	0.24	42	27
…	60	40	4.1	6.7	1.14	32.0	0.19	20	24
…	60	40	5.0	6.7	1.14	32.0	0.19	30	29
…	60	40	6.0	6.7	1.14	32.0	0.19	44	35
…	60	45	3.9	5.3	1.13	32.0	0.15	18	28
…	60	45	5.0	5.3	1.13	32.0	0.15	30	36
…	60	45	6.0	5.3	1.13	32.0	0.15	43	43
…	70	25	4.0	25.1	1.17	33.1	0.69	19	6
…	70	25	5.1	25.1	1.17	33.1	0.69	31	8
…	75	30	4.3	55.3	1.20	35.8	1.44	21	3
…	75	30	5.9	55.3	1.20	35.8	1.44	40	4
10	…	25	4.0	6.0	1.30	45.3	0.13	16	29
10	…	25	4.9	6.0	1.30	45.3	0.13	23	36
10	…	25	5.9	6.0	1.30	45.3	0.13	34	43
15	…	25	4.1	11.0	1.48	44.8	0.23	19	19
15	…	25	5.0	11.0	1.48	44.8	0.23	28	23
15	…	25	5.9	11.0	1.48	44.8	0.23	39	27
15	…	35	4.0	8.6	1.47	44.2	0.18	18	23
23	…	25	…	39.6	1.76	44.1	0.77	…	…
23	…	40	…	24.8	1.74	42.0	0.50	…	…

[a]For loaded model fluids.
[b]For unloaded model fluids.
[c]Jetting velocity at ∼1 mm below the nozzle plane.

diameter (D_{mid}/D_0) against time is obtained and shown in Fig. 5(a). For the self-thinning process of Newtonian fluids with negligible inertia, gravity, and the axial curvature along the filament, the decay of the mid-filament diameter is predicted to be linear.[43,44] In Fig. 5(a), the 10 and 15 vol. % particle-loading model fluids show a linear delay, while 23 vol. % particle-loading model fluid shows a linear delay during the major part of the thinning but a slower delay toward the breakup ($t \geq 3$ ms). The fluid transient apparent extensional viscosity can be estimated from the rate of thinning of the mid-filament diameter during the self-thinning process, $\eta_E(t) = (2X - 1)\frac{\sigma}{-dD_{mid}(t)/dt}$, where η_E denotes the apparent extensional viscosity and X an adjustable correction factor. X accounts for the effect of inertia, gravity and deviation of the filament from a uniform cylinder and can be obtained from the best fit of the initial linear filament thinning which is expected for an initial Newtonian response of the solvents. For the filament thinning profile shown in Fig. 5(a), we obtained that $X = 0.55$, 0.55, and 0.60 for the model fluids with increasing particle-loading. The relationship of the apparent Trouton ratio ($Tr = \eta_E/\eta_0$, where η_0 denotes the zero shear-rate viscosity) and the Hencky strain [$2ln(D_0/D(t))$] is often used to characterize a fluid. The apparent Trouton ratio is independent of the Hencky strain and has a value of 3 for Newtonian fluids. When there is elasticity in the Newtonian solvent, Tr increases with the Hencky strain. Figures 5(b) and 5(c) show the evolution of the transient Tr and the apparent extensional viscosity, respectively, as a function of the filament thinning Hencky strain. It is clearly shown that the model fluids with 10 and 15 vol. % particle-loadings behaved in a Newtonian manner. For the model fluid with 23 vol. % particle-loading, Newtonian behavior was seen at lower Hencky stain followed by increasing Tr and apparent extensional viscosity at higher Hencky strain. Therefore, the jetting of our model dispersion with 23 vol. % particle-loading would probably be less reliable, which was proved to be true later. We note the disparity between the extensional rates achieved by current commercial rheometers, $O(10^3)$ s^{-1}, and that seen during the ejection of a droplet in inkjet printing, $O(10^4 - 10^5)$ s^{-1}. This means that during the jetting process, the Hencky strain and Tr may be larger than the values shown in Fig. 5.

B. Jetting

1. Influence of particle-loading

Figure 6 shows stroboscopic images of the jetting of the loaded model fluids with increasing particle-loading; double strobes were applied to obtain the jetting velocities at ∼1 mm from the nozzle plane.
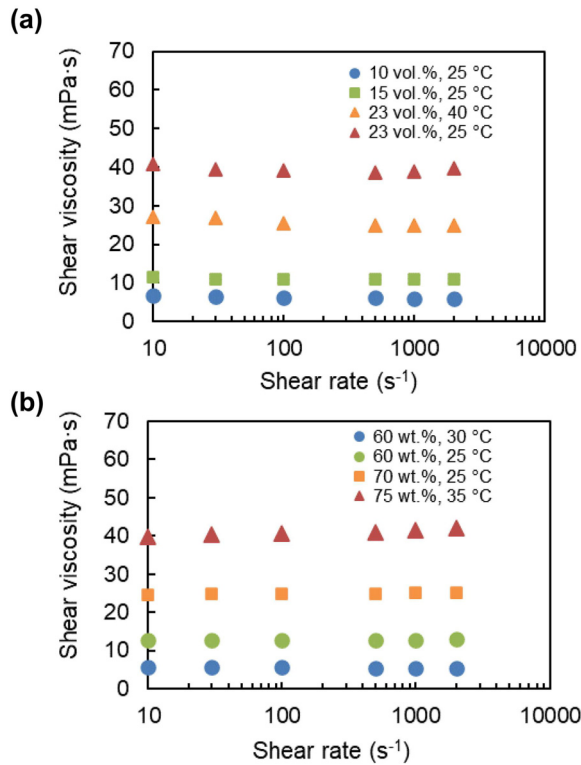
FIG. 2. Shear viscosity profiles of the model fluids. (a) Loaded fluids with different particle-loadings. (b) Unloaded fluids of glycerol/water/5 wt. % 2-butoxyethanol with different glycerol concentrations.

FIG. 3. Viscoelastic moduli of the model fluids at 25 °C. (a) Loaded fluids with different particle-loadings (10, 15, and 23 vol. %). (b) Unloaded fluids of glycerol/water/5 wt. % 2-butoxyethanol with different glycerol concentrations (60, 70, and 75 wt. %).

The jetting was stable and reproducible for lower particle-loadings [see Figs. 6(a) and 6(b)] and became quite unstable for the highest particle-loading of 23 vol. %. As mentioned earlier, the waveform was optimized for individual model fluid in this study to investigate the jettability of model fluids. Despite our best efforts to optimize the waveform for the model fluid with the highest particle-loading, the jetting was unstable. The unstable jetting was most likely related to the fluid properties rather than the waveform used. As presented earlier, this model fluid showed viscoelastic behavior toward the breakup during the thinning process of the filament stretching tests. Local particle–particle interactions in the thin filament formed during the ejection process would result in unreliable breakup of the filament. Also, it was suspected that transient particle–particle interactions inside the nozzle also occurred as unreliable firing and flooding around the nozzle were observed. When particles agglomerate to form a local elastic network inside the nozzle or jamming occurs behind the orifice, some energy would be dissipated to break up the network and the remaining energy not sufficient for the ejected filament breaking to form a droplet, leading to flooding at the nozzle when there is more backflow to the nozzle at the end of a waveform cycle. More unreliable jetting was observed when the jetting temperature was raised to reduce the bulk viscosity of this model fluid. This further excludes high viscosity as the cause of the unstable jetting. At higher temperature with decreased viscosity in the ink channel, stronger Brownian motion of particles can enhance particle–particle interactions, leading to more unstable jetting.
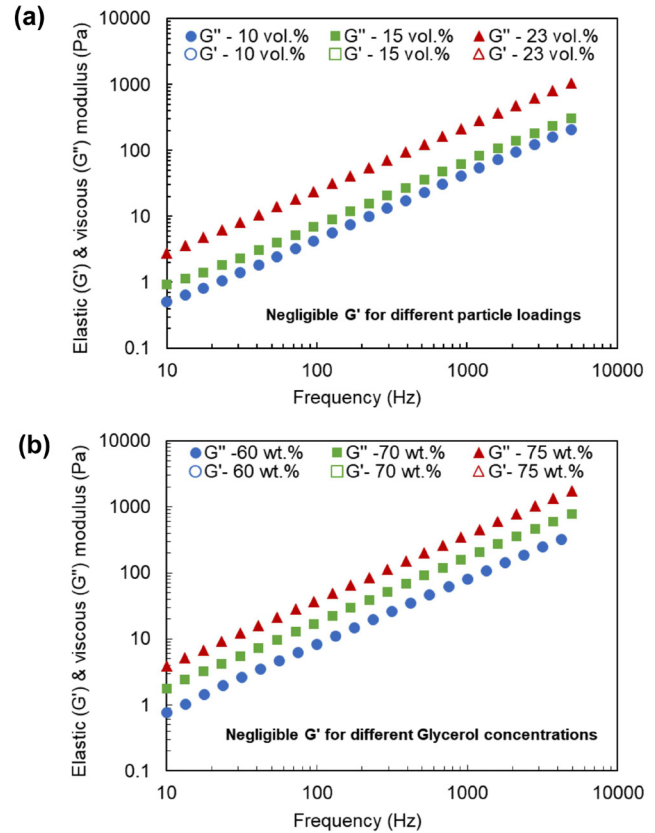
To quantify the reliability of the jetting, 100 stroboscopic images were collected at a frequency of 30 Hz with a jetting frequency of 3000 Hz, and the jetting velocities of 100 different droplets at ~1 mm down the nozzle plane were obtained. Histograms of the jetting velocities (~4 m/s) of the loaded model fluids with 10 and 15 vol. % particles are shown in Fig. 7 as well as an unloaded mode fluids with comparable Oh and We. The jetting of the unloaded model fluid was very reliable, having a standard deviation $SD = 0.02$ m/s for a mean jetting velocity $\bar{V} = 4$ m/s hence a coefficient of variation $C_v = 0.5$ % [see Fig. 7(a)]. With increase in particle-loading, the jetting reliability decreased, having higher coefficients of variation [see Figs. 7(b) and 7(c)]. This is likely due to occasional particle–particle interactions in the thin filament and/or inside the nozzle. At a further higher particle-loading of 23 vol. %, the jetting became too unreliable to obtain reliable droplets [see Fig. 6(c)].

A comparison of the jetting and droplet formation process for an unloaded model fluid and a loaded model fluid at comparable Oh and We is shown in Fig. 8. In general, the jetting behaviors were similar—a droplet with a filament was formed upon ejection from the nozzle, with time the filament further broke into a small satellite which further merged into the major droplet [see Figs. 8(a) and 8(b)]. The jetting process was captured by the high-speed camera and the velocity of the
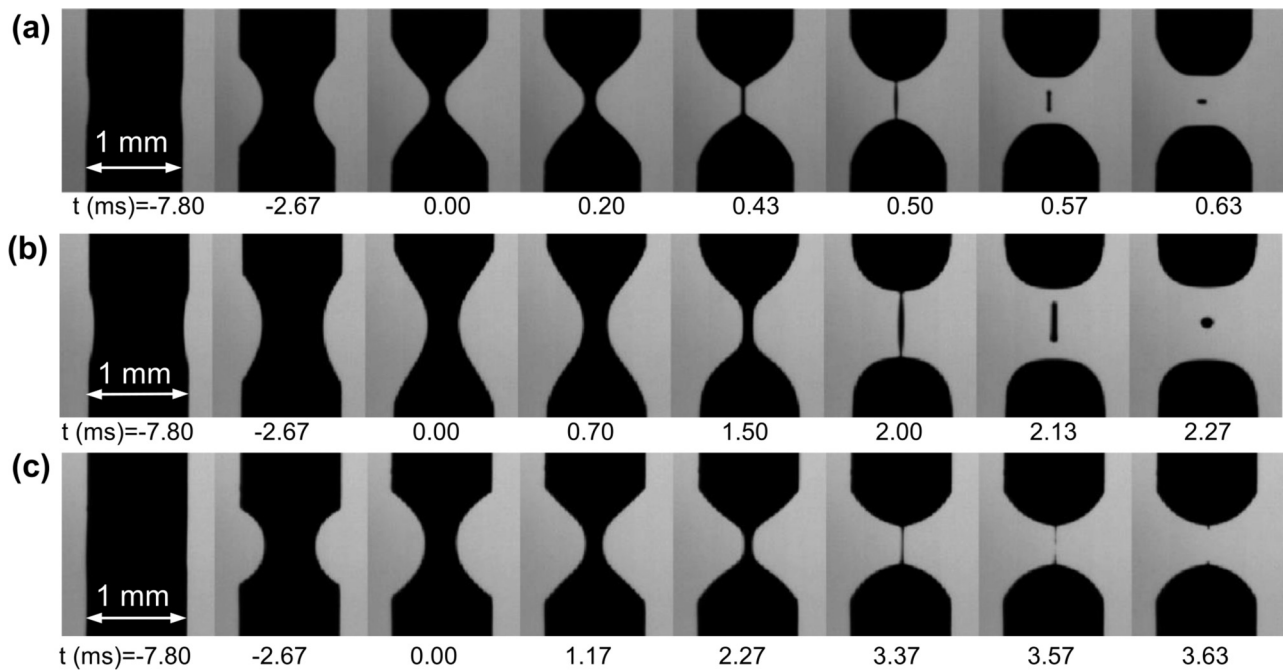
FIG. 4. Sequence of high-speed video images showing filament stretching, thinning and breakup of the model fluids with different particle-loadings [(a) 10, (b) 15, (c) 23 vol. %] at ambient temperature $\sim$22 °C. The piston diameter is 1 mm. Initial sample height of 0.5 mm fluid was stretched to 1.2 mm by moving each piston 0.35 mm apart at a relative stretching velocity of 200 mm/s.

droplet at a specific time can be obtained by extracting the droplet positions in every frame, and further the travel distances in the short time interval of neighboring frames. The inset pictures in Figs. 8(a) and 8(b) show the velocities of the major drop and the filament end where a small bead developed, or the satellite after the filament breaks from the major drop. The velocity of the filament end or the satellite was higher than that of the major drop hence the satellite caught up and merged into the major drop. A difference appeared to be that the loaded model fluid broke up from the nozzle earlier and the filament tail broke up to form a satellite earlier too. Figure 8(c) shows the filament length and mid-filament width with time. Compared to the

unloaded fluid, the loaded fluid broke from the nozzle earlier, forming a drop with a shorter and thicker filament. This filament further broke earlier from the major drop, forming a satellite which merged into the major drop later. The earlier breakup of the filament is likely induced by the particles creating disturbances to the free surface and inducing instability in the thin filament as the filament approaches necking and progresses toward rupture. Earlier breakup and shorter thread lengths for particle-laden suspensions during slow pendant drop formation process have been reported by Furbank and Morris.[47,48] Though the characteristic length in their study is 2 orders larger [millimeter-size drop, particle are $O(100)$ μm and orifices are $O(1)$ mm] than that in
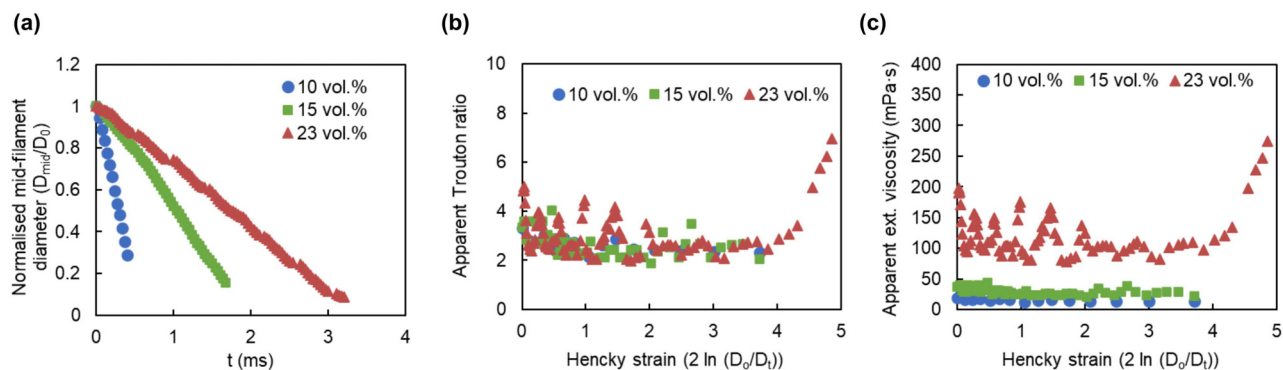

FIG. 5. Normalized filament thinning profile after the cessation of stretching (a), and the evolution of the transient Trouton ratio (b) and the apparent extensional viscosity (c) as a function of the filament thinning Hencky strain.
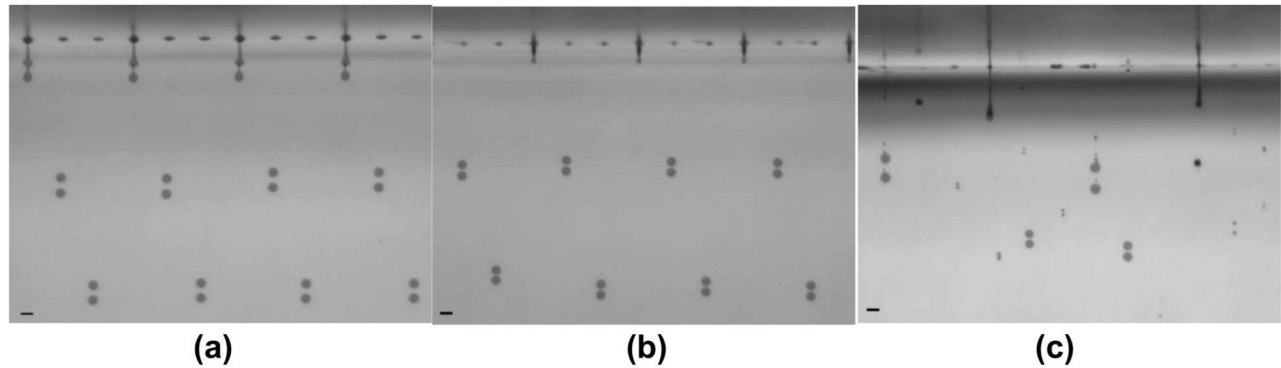
FIG. 6. Overview of the jetting of loaded model fluids with different particle-loadings. (a) 10; (b) 15; (c) 23 vol. %. The pictures were captured by a CCD camera with double strobes. The scale bars represent 50 μm.

our study, the influence of particles on the dynamics of the stretching and thinning of the thread as the rupture is approached is shown to be similar.

2. Influence of Oh and We

Figures 9(a) and 9(b) compare the jetting and droplet formation of the model fluid with 15 vol. % particle-loading at comparable We but different Oh by changing the jetting temperature and hence the fluid viscosity. At similar We, the initial jets coming out of the nozzle were similar ($t \lesssim 34$ ms). For the fluid with lower Oh as shown in Fig. 9(a), necking occurred with time, forming a major drop and a satellite which later merged into the major drop. In contrast, for the fluid with relatively higher Oh as shown in Fig. 9(b), the connection between the filament head and the tail was smoother and the tail merged into the head forming one drop. The filament length of the jet is slightly shorter for the fluid with lower Oh. These are as expected as the relative influence of the viscous force compared to the inertia and surface tension is smaller for the fluid with lower Oh thus its resistance to deformation to form a long jet under inertial force and to form a droplet under surface tension is relatively weaker. Figures 9(b) and 9(c) compare the jetting and droplet formation of the model fluid with 15 vol. % particle-loading at comparable Oh but different We by changing the jetting velocity. Clearly, for the fluid with higher We, the influence of the inertia is stronger, forming a longer and thinner

filament; the thin filament further detached from the major drop before merging back to form a droplet.

3. Jetting maps

The jetting map proposed by Derby[26] was compared with our jetting results. Superimposed upon the jetting map of Derby[26] in Fig. 10(a), represented by the boundary lines, are points from the jetting tests of the unloaded model fluids, and in Fig. 10(b) are points from the jetting tests of the loaded model fluids. These points are also listed in Table I. The typical jetting scenarios observed in our jetting tests are shown in Fig. 10(c). For DOD printing, the most ideal jetting scenario is that there is no satellite upon landing onto the substrate— this could either be no satellite is developed at all as in Fig. 10(c-i) or a satellite develops but soon merges into the major droplet as in Fig. 10(c-ii). These ideal jetting scenarios are located between the boundaries defined by $Oh = 0.1$ and $Oh = 1$ for the unloaded fluids as proposed by Derby.[26] For the loaded fluids, the jetting of the model dispersion with a particle-loading of 23 vol. % with $Oh = 0.8$ and $Oh = 0.5$ at two different temperatures was found to be consistently unreliable with varying jetting velocity or misfiring of droplets. When jetting did not occur reliably, it was not possible to define the jetting velocity, and, hence, Re and We. In the map of Fig. 10(b), the unstable jetting for 23 vol. % particle-loading model fluids is represented by a red shaded region. Compared with unloaded fluids, the jettable region
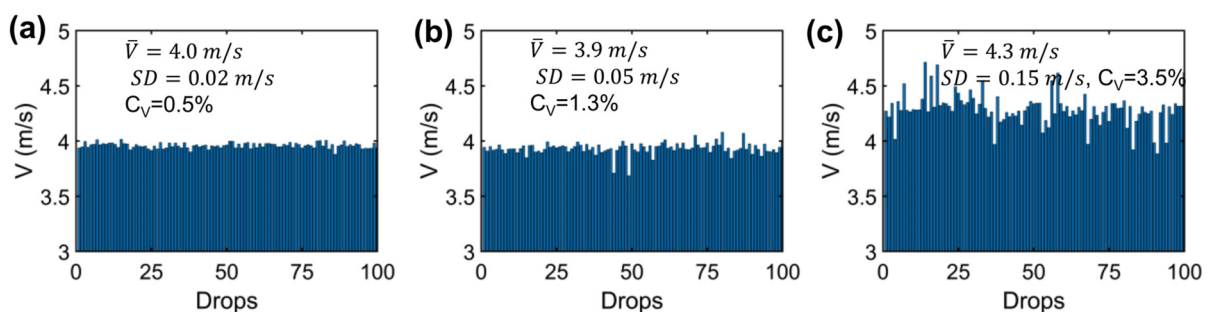

FIG. 7. Histograms of the jetting velocities of different model fluids. (a) Unloaded fluid (glycerol 60 wt. %); (b) loaded fluid—10 vol. % particles; (c) loaded fluid—15 vol. % particles.
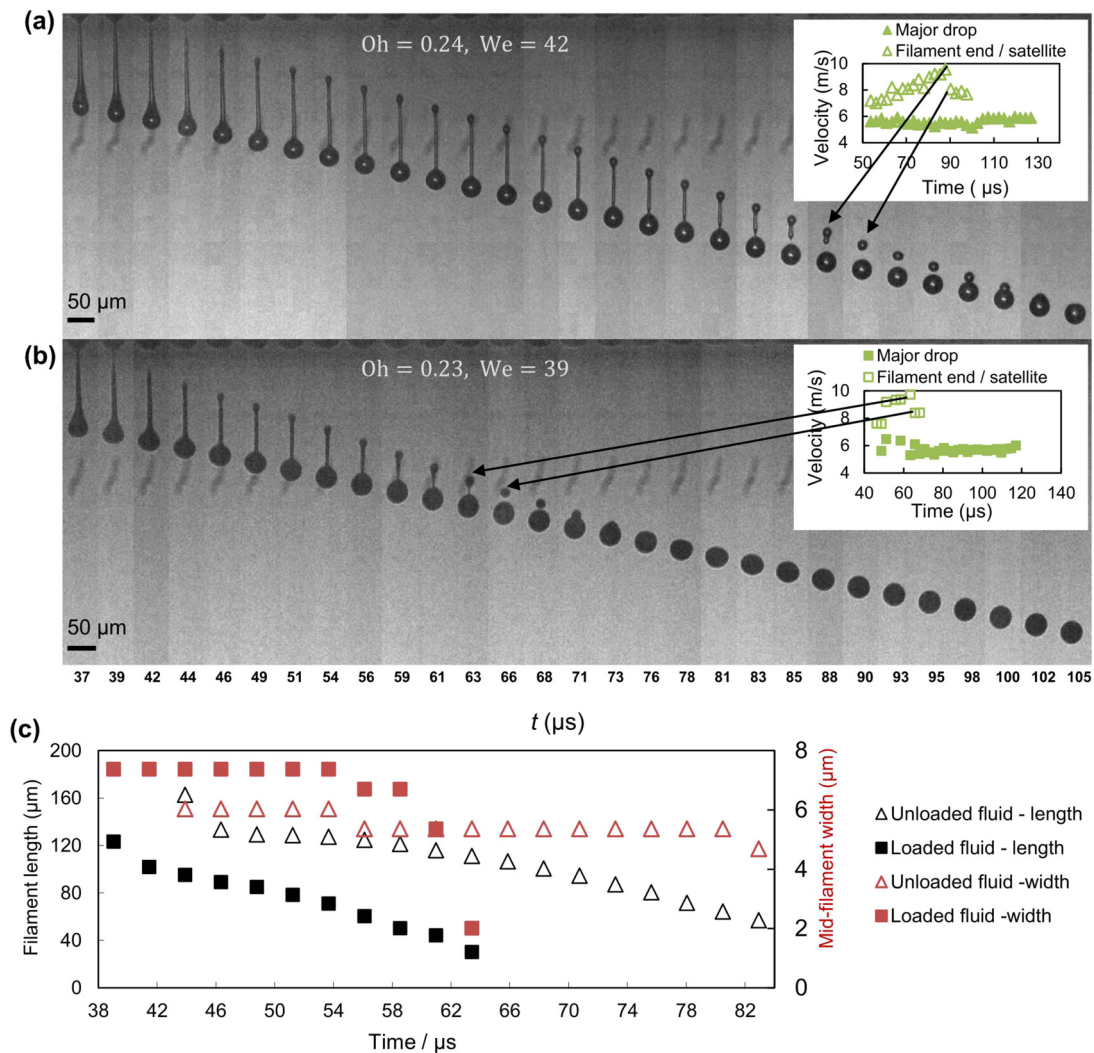
FIG. 8. Sequence of high-speed video images showing the jetting and droplet formation processes of an unloaded model fluid (a) and the loaded model fluid with 15 vol. % particles (b) at comparable Oh and We; the timeline at the bottom is for both sequences. (c) Profiles of filament length and mid-filament width for the unloaded and loaded fluids shown in Figs. 7(a) and 7(b). The image insets show the speed of the droplet and the speed of the filament's end in term of the time from jetting.

was squeezed with the upper bound of *Oh* decreasing due to the influence of particle-loading. For our tests, the stable jetting region is found at $0.1 < Oh < 0.5$ for particle-loading less than 23 vol. %. We note that the extent of the jettability region is dependent on the dispersion characteristics, such as its rheological properties, the size distribution and shape of the particles, as well as the size of the nozzle. Inks with higher particle-loadings (up to 40 vol. %) have been successfully jetted.[1,2] The modified map in Fig. 10(b) is to illustrate the influence of particle-loading in reducing the jettability region for loaded fluids, rather than to give a definite upper bound for loaded fluids as for the unloaded fluids. Therefore, we use a double arrow with opposite directions to indicate that the exact upper boundary can shift toward a lower or higher value of *Oh* for different dispersions and/or printheads.

Within the jettable region, close to the lower boundary of $Oh = 0.1$ and at high *We* (~40) in both Figs. 10(a) and 10(b), a jetting

scenario is observed in which a satellite is developed and flies at the same velocity as the major drop thus the satellite does not merge with the major drop. This jetting scenario is normally not good for inkjet printing applications as the satellite reduces print quality. The transition from ideal jetting to "one satellite, not merging" was only observed at low *Oh* in our study with the investigated velocity range between 4 and 6 m/s. This indicates that the transition from ideal jetting to non-merging one satellite is delayed to a higher *We* at higher *Oh*. This is consistent with the experimental results of Liu and Derby,[29] who also reported the transition from one satellite to multiple satellites, which mainly located in the region of "satellite droplets" with $Oh < 0.1$. As our data are limited with $Oh > 0.1$, such transition was not observed in our experiments. The formation of multiple satellites or "major drop with mist" as we described for unloaded fluids is located outside the normal jettable region at $Oh > 1$ as shown in Fig. 10(a). This scenario
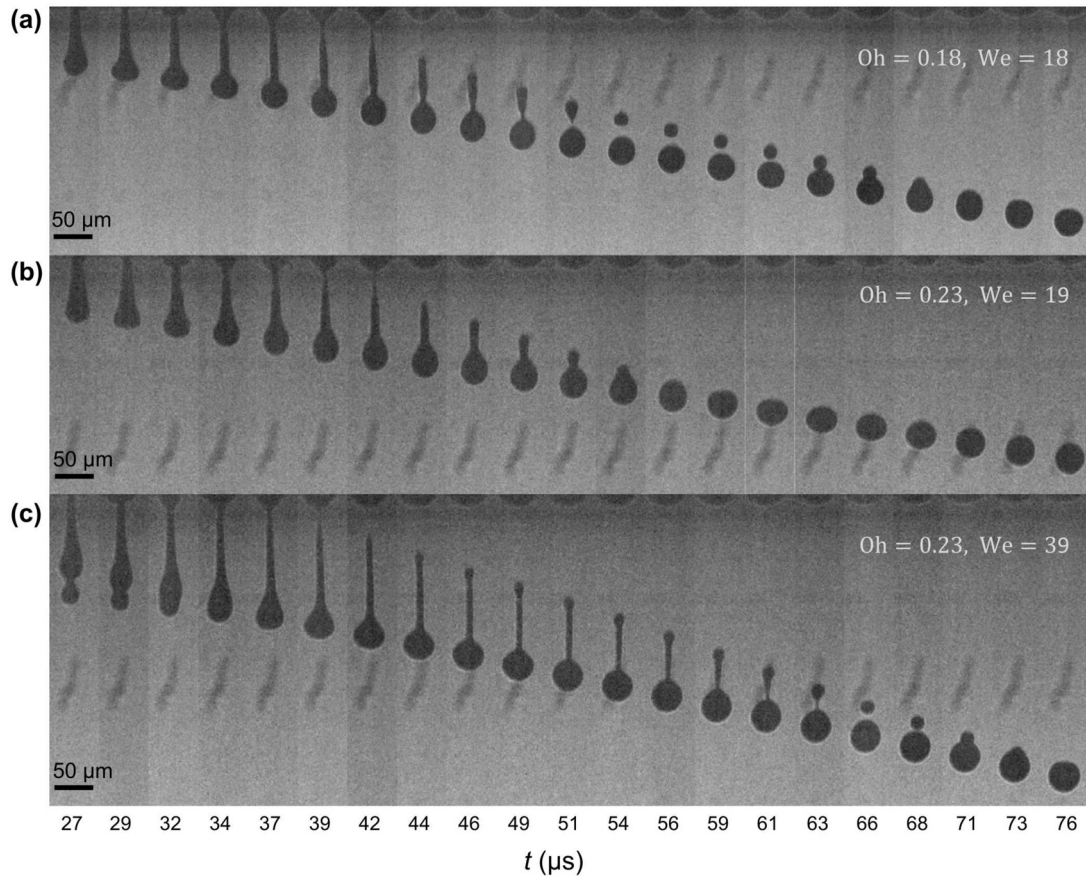
04 June 2024 13:58:28

FIG. 9. Sequence of high-speed video images showing the jetting and droplet formation processes of the loaded model fluids with 15 vol. % particles. (a) $\mu = 8.5$ cP (T = 35 °C), $V = 4$ m/s; (b) $\mu = 11$ cP (T = 25 °C), $V = 4$ m/s; (c) $\mu = 11$ cP (T = 25 °C), $V = 6$ m/s.

is observed for viscous fluid in which a very long and thin filament is formed which further breaks into several tiny droplets (mist) [see Fig. 10(c-iv)]. For some applications where the printing precision requirement is not high, this kind of printing could be acceptable.

For the loaded fluids at low Oh ($\sim$0.1) and low We ($\sim$15) within the jettable region, we also observed the formation of a tiny satellite droplet as the filament gets detached from the nozzle plane to form a major drop [see Fig. 10(c-v)]. This was not observed at comparable Oh and We for the unloaded fluid. During the necking process, individual or groups of particles may be captured in the thread, resulting in the formation of satellites.

The data in Fig. 10 demonstrate the additional complexity that is introduced to the fluid mechanics when particle-loading is increased beyond the dilute regime. Our results also indicate that such levels of particle-loading have a negative impact on the reliability and may pose significant challenges in industrial processes.

IV. CONCLUSION

The ability of inkjet technology to accurately print inks with high particle-loading has opened up a wide range of new applications, including the printing of ceramics, glass, and electronics. However, the potential of this technology is currently limited by our relatively poor

understanding of the impact of the rheology of highly loaded fluids on the printing process. Here, we explored the influence of particle-loading and the complex rheological behavior caused by particle-loading on the jetting and droplet formation process in DOD printing. For particle-loading inks, particle-particle interactions affect the rheological behavior and the jetting performance at a certain range of particle concentration. For our model fluids with different particle-loadings (10, 15, and 23 vol. %), we found that the jetting reliability decreased with increase in the particle-loading and the jetting became very unstable at 23 vol. %. The filament stretching and thinning test for the 23 vol. % particle-loading fluid indicted non-Newtonian behavior at high extensional strain. This shows that the extensional rheology of an ink is an important parameter to guide formulating inks for inkjet printing.

For low particle concentrations, droplet formation is generally similar to those of unloaded inks, provided their Ohnesorge number and Weber number are matched. However, earlier breakup and shorter thread lengths were observed for the loaded fluids, largely due to the instability induced by the particles in the thin filament as the filament approaches necking and progresses toward rupture. A jetting map for loaded fluids indicating the influences of particle-loadings was produced, showing a squeezed jettability region. The jettability region
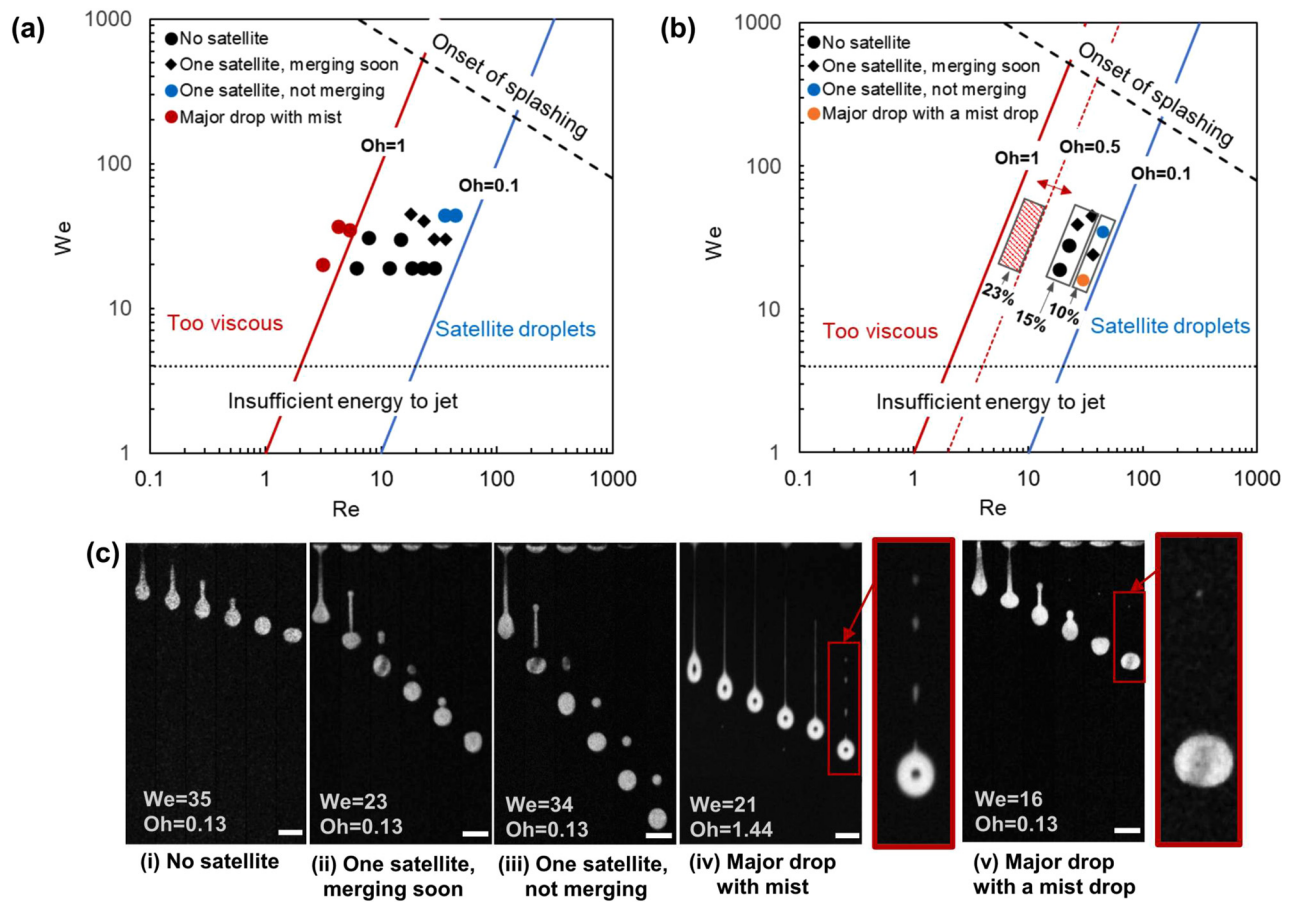
FIG. 10. (a) Comparison of the jetting test results for the unloaded fluids (represented by the markers) with the jetting map of Derby[26] (represented by the boundary lines). (b) Modified jetting map for loaded model fluids. The red shaded region represents unstable jetting for 23 vol. % particle-loading model fluids; the red dash line indicates the upper boundary of Oh for the jettable region of our loaded model fluids and the double arrows indicates this boundary might shift toward a lower or a higher Oh as it is dependent on the properties of dispersions. (c) The typical jetting scenarios in (a) and (b). The scale bars represent 50 μm.

was found at $0.1 < Oh < 0.5$ for our loaded model fluids, compared to $0.1 < Oh < 1$ for unloaded fluids. It is worth remarking that due to the complexity of dispersion systems introduced by the particles, such as the complex rheology and introduced instability on the filament which is related to the particle size, shape, and loading, the boundary of the jettability region for loaded fluids is most likely system (dispersion-printhead)-dependent. Demonstrating the influences of particle-loading on the jetting and droplet formation, we have gained an improved understanding of the jetting of loaded fluids and provided some guide on formulating dispersion inks though significant challenges are there.

AUTHOR DECLARATIONS
Conflict of Interest

The authors have no conflicts to disclose.

Author Contributions

Jing Shi: Investigation (equal); Visualization (equal); Writing – original draft (equal); Writing – review & editing (equal). **Neil Cagney:** Conceptualization (equal); Funding acquisition (equal); Investigation (equal); Supervision (equal); Writing – original draft (equal); Writing – review & editing (equal). **John Tatum:** Funding acquisition (equal); Investigation (equal); Project administration (equal); Writing – original draft (equal); Writing – review & editing (equal). **Angus Condie:** Conceptualization (equal); Funding acquisition (equal); Investigation (equal); Project administration (equal); Writing – original draft

DATA AVAILABILITY

The data that support the findings of this study are available from the corresponding author upon reasonable request.

REFERENCES

[1] K. A. Seerden, N. Reis, J. R. Evans, P. S. Grant, J. W. Halloran, and B. Derby, "Ink-jet printing of wax-based alumina suspensions," J. Am. Ceram. Soc. **84**, 2514–2520 (2001).

[2] T. Wang and B. Derby, "Ink-jet printing and sintering of PZT," J. Am. Ceram. Soc. **88**, 2053–2058 (2005).

[3] B. Derby, "Inkjet printing ceramics: From drops to solid," J. Eur. Ceram. Soc. **31**, 2543–2550 (2011).

[4] H. Sirringhaus, T. Kawase, R. Friend, T. Shimoda, M. Inbasekaran, W. Wu, and E. P. Woo, "High-resolution inkjet printing of all-polymer transistor circuits," Science **290**, 2123–2126 (2000).

[5] B. K. Park, D. Kim, S. Jeong, J. Moon, and J. S. Kim, "Direct writing of copper conductive patterns by ink-jet printing," Thin Solid Films **515**, 7706–7711 (2007).

[6] H. Ning, R. Tao, Z. Fang, W. Cai, J. Chen, Y. Zhou, Z. Zhu, Z. Zheng, R. Yao, M. Xu *et al.*, "Direct patterning of silver electrodes with 2.4 μm channel length by piezoelectric inkjet printing," J. Colloid Interface Sci. **487**, 68–72 (2017).

[7] S. Chung, K. Cho, and T. Lee, "Recent progress in inkjet-printed thin-film transistors," Adv. Sci. **6**, 1801445 (2019).

[8] O. Song, D. Rhee, J. Kim, Y. Jeon, V. Mazánek, A. Söll, Y. A. Kwon, J. H. Cho, Y.-H. Kim, Z. Sofer *et al.*, "All inkjet-printed electronics based on electrochemically exfoliated two-dimensional metal, semiconductor, and dielectric," npj 2D Mater. Appl. **6**, 64 (2022).

[9] J. Hong, Y. Jin, Y. Jin, Y. Li, J. Liu, and J. Chen, "Spread and retraction dynamics of droplet coalescence on a rectangular pixel for organic light-emitting diode inkjet printing," Phys. Fluids **35**, 072014 (2023).

[10] P. C. Rijo, J. M. Cremonezzi, R. J. Andrade, and F. J. Galindo-Rosales, "Correlation between the rheology of electronic inks and the droplet size generated from a capillary nozzle in dripping regime," Phys. Fluids **35**, 093116 (2023).

[11] K. Sen, A. Manchanda, T. Mehta, A. W. Ma, and B. Chaudhuri, "Formulation design for inkjet-based 3D printed tablets," Int. J. Pharm. **584**, 119430 (2020).

[12] R. Walczak and K. Adamski, "Inkjet 3D printing of microfluidic structures-on the selection of the printer towards printing your own microfluidic chips," J. Micromech. Microeng. **25**, 085013 (2015).

[13] J. Li, F. Rossignol, and J. Macdonald, "Inkjet printing for biosensor fabrication: Combining chemistry and technology for advanced manufacturing," Lab Chip **15**, 2538–2558 (2015).

[14] N. C. Martins, S. Fateixa, T. Fernandes, H. I. Nogueira, and T. Trindade, "Inkjet printing of Ag and polystyrene nanoparticle emulsions for the one-step fabrication of hydrophobic paper-based surface-enhanced Raman scattering substrates," ACS Appl. Nano Mater. **4**, 4484–4495 (2021).

[15] Y. Wang, R. Deng, L. Yang, and C. D. Bain, "Fabrication of monolayers of uniform polymeric particles by inkjet printing of monodisperse emulsions produced by microfluidics," Lab Chip **19**, 3077–3085 (2019).

[16] M. Nakamura, A. Kobayashi, F. Takagi, A. Watanabe, Y. Hiruma, K. Ohuchi, Y. Iwasaki, M. Horie, I. Morita, and S. Takatani, "Biocompatible inkjet printing technique for designed seeding of individual living cells," Tissue Eng. **11**, 1658–1666 (2005).

[17] T. Boland, T. Xu, B. Damon, and X. Cui, "Application of inkjet printing to tissue engineering," Biotechnol. J. **1**, 910–917 (2006).

[18] Q. Wang, Y. Liao, Y. Ho, K. Wang, W. Jin, Y. Guan, and W. Fu, "A study on cell viability based on thermal inkjet three-dimensional bioprinting," Phys. Fluids **35**, 082007 (2023).

[19] J. Fromm, "Numerical calculation of the fluid dynamics of drop-on-demand jets," IBM J. Res. Dev. **28**, 322–333 (1984).

[20] B. Derby and N. Reis, "Inkjet printing of highly loaded particulate suspensions," MRS Bull. **28**, 815–818 (2003).

[21] D. Jang, D. Kim, and J. Moon, "Influence of fluid physical properties on ink-jet printability," Langmuir **25**, 2629–2635 (2009).

[22] K. San, J. H. Choi, D. K. Sohn, and H. S. Ko, "Printability of inkjet according to supply pressure," Phys. Fluids **35**, 053304 (2023).

[23] H. Wickström, E. Hilgert, J. O. Nyman, D. Desai, D. Şen Karaman, T. De Beer, N. Sandler, and J. M. Rosenholm, "Inkjet printing of drug-loaded mesoporous silica nanoparticles—A platform for drug development," Molecules **22**, 2020 (2017).

[24] A. A. Castrejón-Pita, E. S. Betton, N. Campbell, N. Jackson, J. Morgan, T. R. Tuladhar, D. C. Vadillo, and J. R. Castrejon-Pita, "Formulation, quality, cleaning, and other advances in inkjet printing," Atomization Sprays **31**, 57 (2021).

[25] H. C. Nallan, J. A. Sadie, R. Kitsomboonloha, S. K. Volkman, and V. Subramanian, "Systematic design of jettable nanoparticle-based inkjet inks: Rheology, acoustics, and jettability," Langmuir **30**, 13470–13477 (2014).

[26] B. Derby, "Inkjet printing of functional and structural materials: Fluid property requirements, feature stability, and resolution," Annu. Rev. Mater. Res. **40**, 395–414 (2010).

[27] G. H. McKinley and M. Renardy, "Wolfgang von Ohnesorge," Phys. Fluids **23**, 127101 (2011).

[28] D. Lohse, "Fundamental fluid dynamics challenges in inkjet printing," Annu. Rev. Fluid Mech. **54**, 349–382 (2022).

[29] Y. Liu and B. Derby, "Experimental study of the parameters for stable drop-on-demand inkjet performance," Phys. Fluids **31**, 032004 (2019).

[30] H. J. Shore and G. M. Harrison, "The effect of added polymers on the formation of drops ejected from a nozzle," Phys. Fluids **17**, 033104 (2005).

[31] B.-J. de Gans, L. Xue, U. S. Agarwal, and U. S. Schubert, "Ink-jet printing of linear and star polymers," Macromol. Rapid Commun. **26**, 310–314 (2005).

[32] I. Hutchings, T. Tuladhar, M. Mackley, D. Vadillo, S. Hoath, and G. Martin, "Links between ink rheology, drop-on-demand jet formation, and printability," J. Imaging Sci. Technol. **53**, 041208 (2009).

[33] S. D. Hoath, O. G. Harlen, and I. M. Hutchings, "Jetting behavior of polymer solutions in drop-on-demand inkjet printing," J. Rheol. **56**, 1109–1127 (2012).

[34] H. Yoo and C. Kim, "Generation of inkjet droplet of non-Newtonian fluid," Rheol. Acta **52**, 313–325 (2013).

[35] C. Slade, "Freeforming ceramics using a thermal jet printer," J. Mater. Sci. Lett. **17**, 1669–1671 (1998).

[36] E. Özkol, J. Ebert, K. Uibel, A. Wätjen, and R. Telle, "Development of high solid content aqueous 3Y-TZP suspensions for direct inkjet printing using a thermal inkjet printer," J. Eur. Ceram. Soc. **29**, 403–409 (2009).

[37] M. Grouchko, A. Kamyshny, and S. Magdassi, "Formation of air-stable copper–silver core–shell nanoparticles for inkjet printing," J. Mater. Chem. **19**, 3057–3062 (2009).

[38] X. Wang, W. W. Carr, D. G. Bucknall, and J. F. Morris, "Drop-on-demand drop formation of colloidal suspensions," Int. J. Multiphase Flow **38**, 17–26 (2012).

[39] S. Abbott, "Practical formulation science for particle-based inks," Colloids Interfaces **3**, 23 (2019).

[40] A. van der Bos, M.-J. van der Meulen, T. Driessen, M. van den Berg, H. Reinten, H. Wijshoff, M. Versluis, and D. Lohse, "Velocity profile inside piezoacoustic inkjet droplets in flight: Comparison between experiment and numerical simulation," Phys. Rev. Appl. **1**, 014004 (2014).

[41] S. Mueller, E. Llewellin, and H. Mader, "The rheology of suspensions of solid particles," Proc. R. Soc. A. **466**, 1201–1228 (2010).

[42] A. Condie and J. Brünahl, "Xaar's inkjet printing technology and applications," in *Inkjet Printing in Industry*, edited by W. Zapka (John Wiley & Sons, 2022), Chap. 21, pp. 535–554.

[43] G. H. McKinley, "Visco-elasto-capillary thinning and break-up of complex fluids," in *Rheology Reviews* (British Society of Rheology, Aberystwyth, 2005), pp. 1–49.

04 June 2024 13:58:28

[44]T. Tuladhar and M. Mackley, "Filament stretching rheometry and break-up behaviour of low viscosity polymer solutions and inkjet fluids," J. Non-Newtonian Fluid Mech. **148**, 97–108 (2008).

[45]D. Vadillo, T. Tuladhar, A. Mulji, S. Jung, S. Hoath, and M. Mackley, "Evaluation of the inkjet fluid's performance using the 'Cambridge Trimaster' filament stretch and break-up device," J. Rheol. **54**, 261–282 (2010).

[46]G. H. McKinley and T. Sridhar, "Filament-stretching rheometry of complex fluids," Annu. Rev. Fluid Mech. **34**, 375–415 (2002).

[47]R. J. Furbank and J. F. Morris, "An experimental study of particle effects on drop formation," Phys. Fluids **16**, 1777–1790 (2004).

[48]R. J. Furbank and J. F. Morris, "Pendant drop thread dynamics of particle-laden liquids," Int. J. Multiphase Flow **33**, 448–468 (2007).

04 June 2024 13:58:28